THE AMERICAN SOCIETY OF MECHANICAL ENGINEERS
345 E. 47th St., New York, N.Y. 10017

97-GT-207

VISCOUS FLOW FIELD COMPUTATIONS FOR A TRANSONIC AXIAL–FLOW COMPRESSOR BLADE USING DIFFERENT TURBULENCE MODELS

L. J. Lenke and H. Simon
Institute of Turbomachinery
University of Duisburg
47048 Duisburg
Germany

ABSTRACT

New blading concepts as used in modern transonic axial–flow compressors require improved calculation methods. Here the turbulence modelling has great influence. Therefore a quasi-three-dimensional compressor blade with subsonic inlet conditions is calculated using different turbulence models. A low-Reynolds number k-ϵ, the k-ω model and an explicit algebraic Reynolds stress model are considered in this investigation.

The results from these calculations in form of comparisons between the predicted isentropic Mach number distributions, profile losses and exit flow angles with experimental data are presented in this paper. They demonstrate the differences between the models in the prediction of the separation behavior of blade surface boundary layer especially which are introduced by shocks. For the high inlet Mach numbers the models differ also in the prediction of losses and deviation angles at design and off–design conditions.

INTRODUCTION

Modern axial-flow compressors are characterized by high efficiency and minimum size or a maximized massflow. To satisfy these requirements, the blade rows of the compressor stages must be designed as to provide the largest possible working range between choking and near stall at highest inlet Mach numbers. While high inlet Mach numbers reduce the unit size, any transonic inlet flow causes additional losses by shock waves and narrows the working range. This leads to blading designs in a small Mach number range, where the influence on profile losses is comparatively high.

Transferred these demands to the cascade design, modern design methods have to be used for the profile development to permit the prescribed velocity distribution inside the blade passage. These methods to solve the flow field equations can be divided into direct and inverse calculation methods. The inverse calculation method based on a given velocity distribution will be preferred if a completely new cascade design is to be developed and no experience is available with the cascade configuration. The direct method will be preferred if the profile geometry must be modified or to determine the off-design performance (Weber et al., 1986).

The high inlet Mach numbers cause compression shocks at the suction side and flow separation results from interactions of the shocks with the boundary layers. For a precise determination of all these effects there are high requirements to direct calculation programs. However, some critical items limit the effectiveness of these programs. Chief among these items is turbulence modeling.

Reynolds stress models represent the highest level of closure that is currently feasible for practical calculations. These models are superior to the well-known two-equation models, but many unknown turbulent quantities are required. However, these models could be used to derive new two-equation models.

In this paper, two explicit algebraic stress models (ASM) from Abid et al. (1995) are compared with the $k-\epsilon$ model from Lam and Bremhorst (1981) and the $k-\omega$ model from Wilcox (1993). The ability of the models to predict the transonic flow through the SKG-FVV 3.3 cascade investigated by Weber et al. (1986) is evaluated systematically, including the influence of the axial velocity density ratio (AVDR). A selection of different incidences are compared

Presented at the International Gas Turbine & Aeroengine Congress & Exhibition
Orlando, Florida — June 2–June 5, 1997

CFL	Courant number
$c_{\epsilon 1}, c_{\epsilon 2}, c_\mu$	coefficients in the k-ϵ model
f_1, f_2, f_2^*, f_μ	damping functions in the k-ϵ model
f_C, f_{Ck}	coefficients for local variable CFL numbers
k	turbulent kinetic energy
l	blade chord
M	Mach number
M_{is}	isentropic Mach number
P	production term of turbulent kinetic energy
R_T, R_y	turbulent Reynolds numbers
S	mean rate of strain
t	time
$\bar{u}$	mean velocity
W	vorticity tensor
x	coordinate in chordwise direction
y	distance from the wall
$\alpha_{1\ldots5}$	coefficients of the ASM model
$\alpha, \alpha^*, \beta, \beta^*$	coefficients in the k-ω model
β	flow angle
$\delta_{\cdot}$	kronecker delta
ϵ	dissipation rate of turbulence energy
η	strain rate invariant
μ	molecular viscosity
μ_t	turbulent viscosity
$\bar{\rho}$	mean density
$\sigma_k, \sigma_\epsilon, \sigma_\omega$	turbulent Prandtl nnmbers for diffusion of k, ϵ and ω
τ	Reynolds stress tensor
ξ	strain rate invariant
ζ	total pressure loss coefficient $= (p_{t1} - p_{t2})/(p_{t1} - p_1)$
Ω	axial velocity density ratio (AVDR)
ω	specific dissipation rate

Subscripts

i, j	tensor notation
1	inlet plane
2	outlet plane

Table 1: Nomenclature

with measurements to illustrate the differences between the turbulence models.

THE NUMERICAL SCHEME

Low-Reynolds-Number k-ϵ Model (LB-model)

The Standard k-ϵ model uses the Boussinesq eddy viscosity concept and neglects the molecular diffusion compared to turbulent diffusion so that this high-Reynolds-number form of the k-ϵ model is not valid in the vicinity of solid walls. In the low-Reynolds-number form of the k-ϵ model devised by Lam & Bremhorst (1981), the viscous effects are accounted for by replacing the original set of constants by functions of the turbulent Reynolds numbers R_T and R_y to integrate the k and ϵ transport equations directly to the wall. This leads to the modeled transport equations

$$\frac{D(\bar{\rho}k)}{Dt} = \frac{\partial}{\partial x_j}\left[\left(\frac{\mu_t}{\sigma_k} + \mu\right)\frac{\partial k}{\partial x_j}\right] + P - \bar{\rho}\epsilon \qquad (1)$$

$$\frac{D(\bar{\rho}\epsilon)}{Dt} = \frac{\partial}{\partial x_j}\left[\left(\frac{\mu_t}{\sigma_\epsilon} + \mu\right)\frac{\partial \epsilon}{\partial x_j}\right] + c_{\epsilon 1} f_1 \frac{\epsilon}{k} P - c_{\epsilon 2}\bar{\rho} f_2 \frac{\epsilon^2}{k} \qquad (2)$$

with the production term $P = -\bar{\rho}\tau_{ij}(\partial \bar{u}_i/\partial x_j)$ of the turbulent energy, the Reynolds stress tensor τ_{ij} and the turbulent viscosity μ_t

$$\tau_{ij} = \mu_t\left(\frac{\partial \bar{u}_i}{\partial x_j} + \frac{\partial \bar{u}_j}{\partial x_i} - \frac{2}{3}\frac{\partial \bar{u}_k}{\partial x_k}\delta_{ij}\right) - \frac{2}{3}\bar{\rho}k\delta_{ij} \qquad (3)$$

$$\mu_t = c_\mu \bar{\rho}\frac{k^2}{\epsilon} \qquad (4)$$

The coefficients of the model are

$c_{\epsilon 1}$	$c_{\epsilon 2}$	c_μ	σ_k	σ_ϵ
1.44	1.92	0.09	1.3	1.0

and the damping functions

$$f_1 = 1 + (0.05/f_\mu)^3 \qquad (5)$$

$$f_2 = 1 - f_2^* \exp(-R_T^2) \qquad (6)$$

$$f_2^* = \max(0.95; 1 - \tanh[(\max[0; f_\mu - 1])^2]) \qquad (7)$$

$$f_\mu = [1 - \exp(-0.0165 R_y)]^2 (1 + 20.5/R_T) \qquad (8)$$

$$R_T = \bar{\rho}\frac{k^2}{\epsilon\mu}, \qquad R_y = \bar{\rho}\frac{y\sqrt{k}}{\mu} \qquad (9)$$

The function f_2^* limits the function f_2 to a minimum value and avoids very small values of k so that higher Courant numbers (Courant et al., 1928) can be used. The function f_2^* has no significant influence on the numerical results but higher convergence rates can be obtained.

At the wall, the boundary conditions for k and ϵ are

$$k = 0, \qquad \frac{\partial \epsilon}{\partial y} = 0 \qquad (10)$$

where $\partial\epsilon/\partial y$ describes the gradient of ϵ normal to the wall.

k–ω Turbulence Model

Unlike any other two-equation model, the k–ω model does not involve damping functions to integrate through the viscous sublayer and allows simple Dirichlet boundary conditions. The modeled transport equations for k and ω suggested by Wilcox (1993) for a low Reynolds number model are

$$\frac{D(\bar{\rho}k)}{Dt} = \frac{\partial}{\partial x_j}\left[\left(\frac{\mu_t}{\sigma_k}+\mu\right)\frac{\partial k}{\partial x_j}\right] + P - \bar{\rho}\beta^*\omega k \qquad (11)$$

$$\frac{D(\bar{\rho}\omega)}{Dt} = \frac{\partial}{\partial x_j}\left[\left(\frac{\mu_t}{\sigma_\omega}+\mu\right)\frac{\partial \omega}{\partial x_j}\right] + \alpha\frac{\omega}{k}P - \beta\bar{\rho}\omega^2 \qquad (12)$$

given that $\mu_t = \alpha^*\bar{\rho}k/\omega$. The closure coefficients of the model are as follows

$$\alpha^* = \frac{\alpha_0^* + R_T/6}{1+R_T/6} \qquad (13)$$

$$\alpha = \frac{5}{9}\frac{\alpha_0 + R_T/2.7}{1+R_T/2.7}\frac{1}{\alpha^*} \qquad (14)$$

$$\beta^* = \frac{9}{100}\frac{5/18+(R_T/8)^4}{1+(R_T/8)^4} \qquad (15)$$

β	α_0^*	α_0	σ_k	σ_ω
3/40	1/40	0.1	2.0	2.0

with the turbulence Reynolds number $R_T = \bar{\rho}k/(\mu\omega)$.

At the wall, the boundary conditions for k and ω are

$$k = 0, \qquad \omega = 10\frac{6\mu}{\beta\bar{\rho}(\Delta y)^2} \qquad (16)$$

where Δy is the distance to the first grid point away from the wall.

Explicit Algebraic Stress Models

In this paper, the algebraic stress equation is applied within the context of the k-ω and k-ϵ two-equation models. Instead of the usual Boussinesq eddy viscosity concept, the nonlinear, explicit algebraic stress model of Abid et al. (1995) will be used, which is given by

$$\bar{\rho}\tau_{ij} = \frac{2}{3}\bar{\rho}k\delta_{ij} - 2\mu_t^*\left[\left(S_{ij}-\frac{1}{3}S_{kk}\delta_{ij}\right) + (\alpha_4/\omega)(S_{ik}W_{kj} + S_{jk}W_{ki}) - (\alpha_5/\omega)(S_{ik}S_{kj} - \frac{1}{3}S_{kl}S_{kl}\delta_{ij})\right] \qquad (17)$$

with

$$\mu_t^* = \bar{\rho}c_\mu^*(k/\omega) \qquad (18)$$

$$c_\mu^* = \frac{3(1+\eta^2)\alpha_1}{3+\eta^2+6\xi^2\eta^2+6\xi^2} \qquad (19)$$

where $\tau_{ij} \equiv \overline{u_i'u_j'}$ is the Reynolds stress tensor and

$$S_{ij} = \frac{1}{2}\left(\frac{\partial \bar{u}_i}{\partial x_j}+\frac{\partial \bar{u}_j}{\partial x_i}\right), \quad W_{ij} = \frac{1}{2}\left(\frac{\partial \bar{u}_i}{\partial x_j}-\frac{\partial \bar{u}_j}{\partial x_i}\right) \qquad (20)$$

are the mean rate of strain and mean vorticity tensors built up from the gradients of the mean velocity field. η and ξ are strain rate invariants defined by

$$\eta = \frac{\alpha_2}{\omega}\sqrt{S_{ij}S_{ij}}, \quad \xi = \frac{\alpha_3}{\omega}\sqrt{W_{ij}W_{ij}} \qquad (21)$$

and the five coefficients

α_1	α_2	α_3	α_4	α_5
0.1067	0.05	0.138	0.138	0.1

The algebraic stress equation (17) must be solved in conjunction with two transport equations. Therefore, two models will be proposed. In model ASM-k-ω, the standard k-ω equations are solved with Eq. (17) and in model ASM-k-ϵ, the standard k-ϵ equations are solved with Eq. (17). In the second model ω in Eq. (17) must be replaced by $\omega = \epsilon/k$.

Both models could be integrated directly to a solid wall if the singularity in the destruction of dissipation term $-c_{\epsilon 2}\epsilon^2/k$ is removed. This leads to Eq. (1)-(2) for k and ϵ with the new damping functions and coefficients

$$f_1 = 1, \qquad f_2 = 1-\exp(-R_y/12.5), \qquad f_\mu = 1 \qquad (22)$$

$c_{\epsilon 1}$	$c_{\epsilon 2}$	c_μ	σ_k	σ_ϵ
1.39	1.83	0.088	1.3	1.0

with the boundary conditions at the wall for k and ϵ suggested by Abid et al. (1995)

$$k = 0, \qquad \epsilon = 2\frac{\mu}{\bar{\rho}}\left(\frac{\partial\sqrt{k}}{\partial y}\right)^2 \qquad (23)$$

and to Eq. (11)-(12) for k and ω with the new coefficients suggested by Abid et al. (1995)

β^*	β	α^*	α	σ_k	σ_ω
1.0	0.83	0.088	0.547	1.4	2.0

with the boundary conditions taken from Eq. 16.

The Discretisation Method

In this investigation a finite volume formulation of the full Navier–Stokes equations is used picking up elements from Roe's and Osher's scheme. Furthermore, only steady state solutions including the influence of the AVDR are considered. For high convergence rates, an implicit, Newton-Raphson-like iterative method is used to solve first the averaged conservation equations and then the modeled transport equations but with different CFL numbers for each set of equations (details described in Lenke et al. (1995) and

Reichert (1995)). Furthermore, the local time step size is calculated using a CFL number, which is a function of the local change of the density given by

$$CFL = CFL_0 \left(1 + (fc - 1)\left[1 - \exp\left(\frac{-1}{5000}\frac{\Delta\bar{\rho}_{max}}{\Delta\bar{\rho}}\right)\right]^2\right) \quad (24)$$

with $fc = 5 \ldots 10$ for higher local CFL numbers.

For solving the k, ϵ and ω equations the local CFL number is a function of the local change of $\bar{\rho}k$ given by

$$CFL = CFL_0 \left(1 + (fc_k - 1)\left[1 - \exp\left(\frac{-1}{5000}\frac{\Delta(\bar{\rho}k)_{max}}{\Delta(\bar{\rho}k)}\right)\right]^2\right) \quad (25)$$

with $fc_k = 1 \ldots 5$.

An example for the influence of Eq. (24) and (25) on the convergence history is shown in Fig 1 for the SKG-FVV 3.3 cascade with an inlet Mach number $M_1 = 0.6$. Both calculations have been done with the k-ω turbulence model and the highest possible CFL_0 number ($CFL_0 = 3$) for all equations. Fig 1 demonstrates the high efficiency of a local variable CFL number especially at the beginning of a calculation but with decreasing residuum the influence of Eq. (24) and (25) will be reduced.

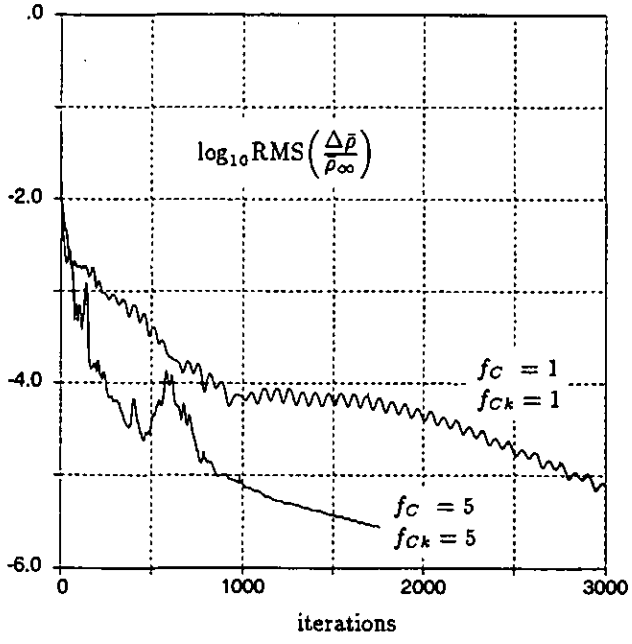

Figure 1: Influence of fc and fc_k on the convergence history, SKG-FVV 3.3 cascade with $M_1 = 0.6$ and k-ω turbulence model

NUMERICAL RESULTS

The calculations to be presented have been done with the different turbulence models for the quasi-three-dimensional flow through the SKG-FVV 3.3 cascade with a design inlet flow angle $\beta_1 = 142°$ and a design inlet Mach number $M_1 = 0.85$. For all calculations shown in this paper the total pressure and temperature were specified at inlet and static pressure at exit but no turbulence intensity or inlet values of k, ϵ or ω were specified because the numerical results have shown no dependence on inlet values.

The Comparisons have been made with the experimental data contained in Jawtusch (1993). In the calculations the distribution of Ω is assumed to be a linear variation between the leading and trailing edges because no details of the Ω distrihution were determined for the actual flow. The computational multiblock mesh is shown in Fig 2 with an enlargement of the trailing edge.

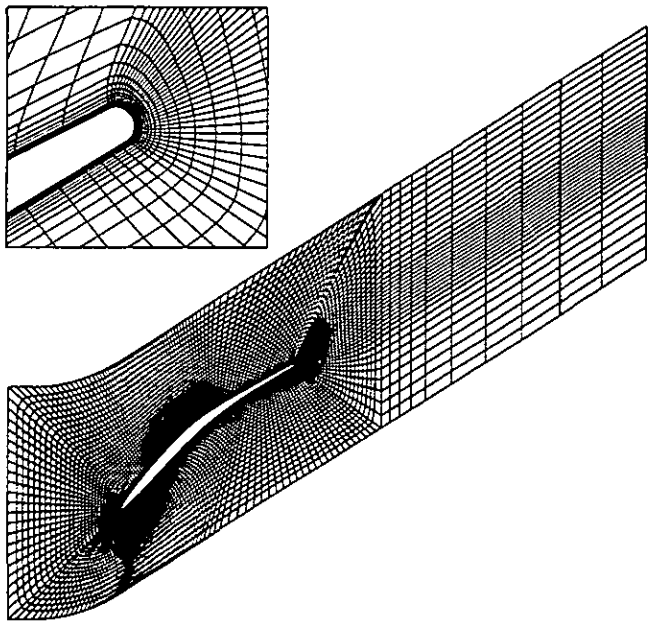

Figure 2: Grid topology for the SKG-FVV 3.3 cascade (10857 gridpoints)

Inlet Mach Number Effect

In addition to the design point the influence of M_1 on the surface Mach number distribution is provided in Fig. (3) for the design incidence. Below the design Mach number at $M_1 = 0.6$ and $M_1 = 0.75$ the turbulence models lie close together and agree well with the measurements. Near the leading edge the predicted isentropic Mach numbers are consistently lower than the measured Mach numbers especially with high inlet Mach numbers. This effect may be due

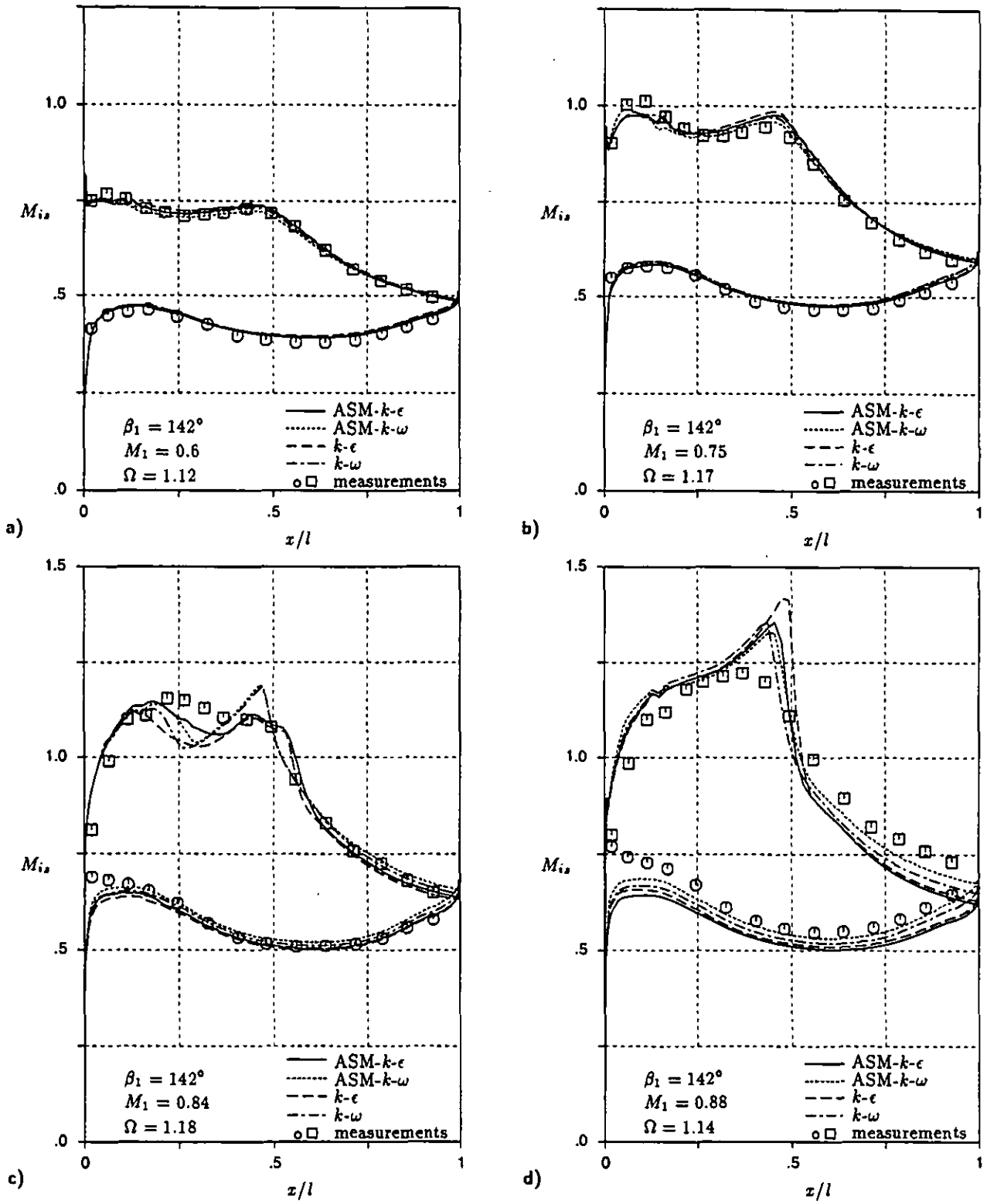

Figure 3: Isentropic surface Mach number distribution at design flow angle and different inlet Mach numbers: (a) $M_1 = 0.6$, (b) $M_1 = 0.75$, (c) $M_1 = 0.84$ and (d) $M_1 = 0.88$

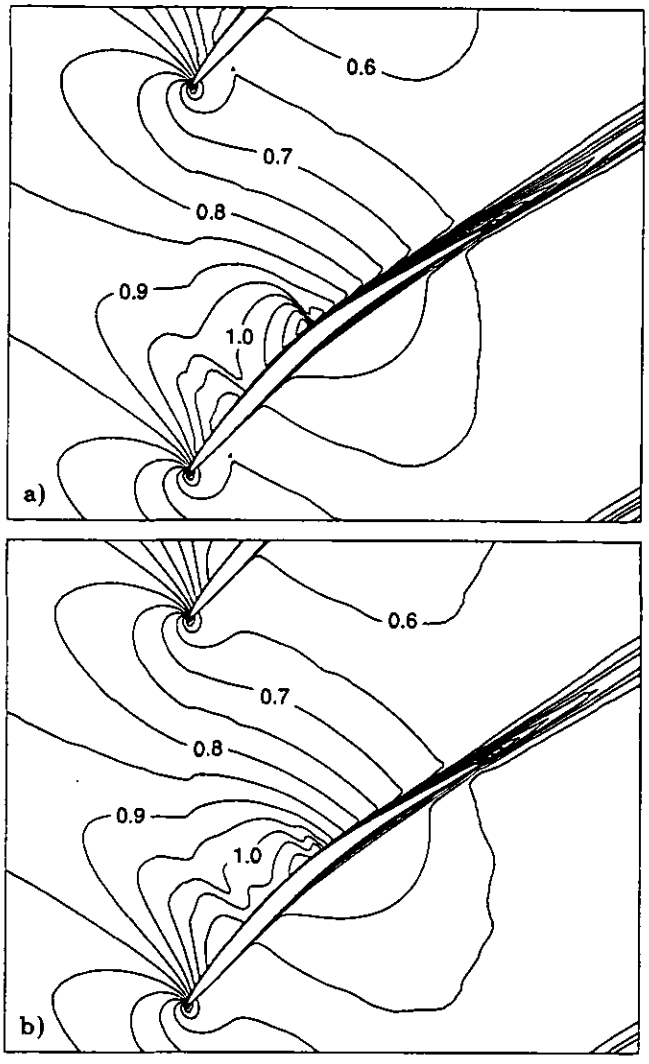

Figure 4: Predicted Mach number distribution at design point: a) k-ω models and b) k-ϵ models

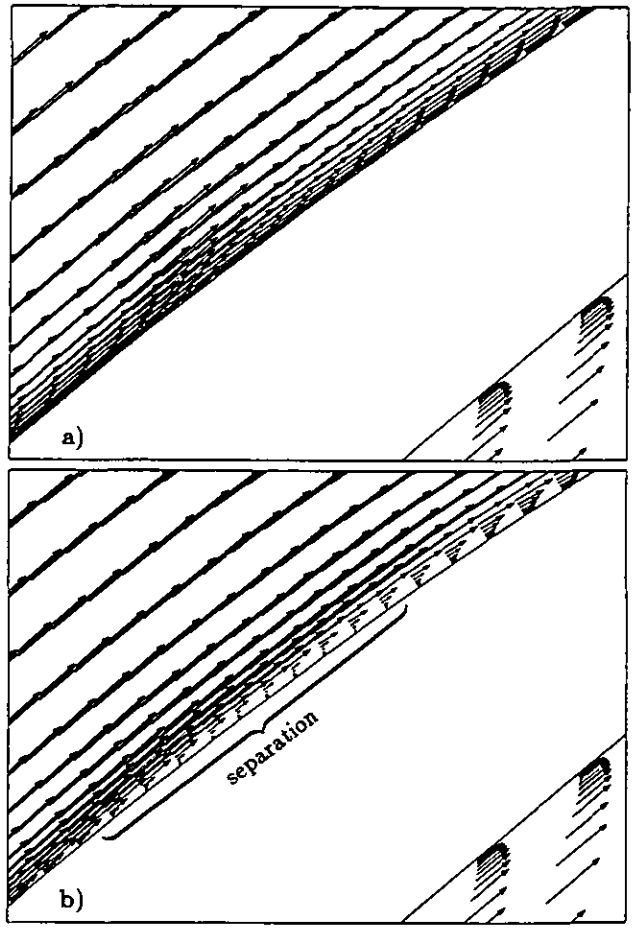

Figure 5: Velocity vectors at approximately 50 percent of chord at design point: a) k-ω models and b) k-ϵ models

to differences between the measured incidence angle and the design incidence angle which is used in the calculations. Another reason could be an incorrect modeled distribution of Ω along the chord lenght. In the measurements only the absolut value of Ω is given. But different investigations have shown, that the distribution of Ω influences the Mach number distribution especially at the leading and trailing edges.

With higher inlet Mach numbers the turhulence models differ more. At design Mach number in Fig. (3c) the turbulence models differ only in the front half of suction side. The k-ω turbulence models calculate a weak shock in the middle of the suction side with a peak in the Mach numher distribution in front of the shock (Fig. (4a)). But the main difference between the models is a closed and very thin separation bubble around 50 percent of chord at suction side which is calculated by the k-ϵ models although these hoth models calculate nearly no shock at suction side (Fig. (5b)). This separation bubble initiates lower isentropic Mach numbers at this location which agree better with the measurements. The ASM-models and the corresponding standard two equation models show the same characteristics in the Mach number distribution and separation behavior.

At $M_1 = 0.88$ all the turbulence models calculate a small shock in the middle of the suction side with a peak in the Mach number distribution in front of the shock but only the k-ϵ models calculate a separation bubble which is quite similar to Fig. (5b). In the rear half of the suction side and at the pressure side the turbulence models show similar Mach number distributions with a vertical displacement. This displacement results from the different loss coefficients calculated by the models.

In Fig. (6a) the dependence of the loss coefficients on the inlet Mach number is presented. It is shown, that the k-ϵ models calculate lower losses compared to the k-ω mod-

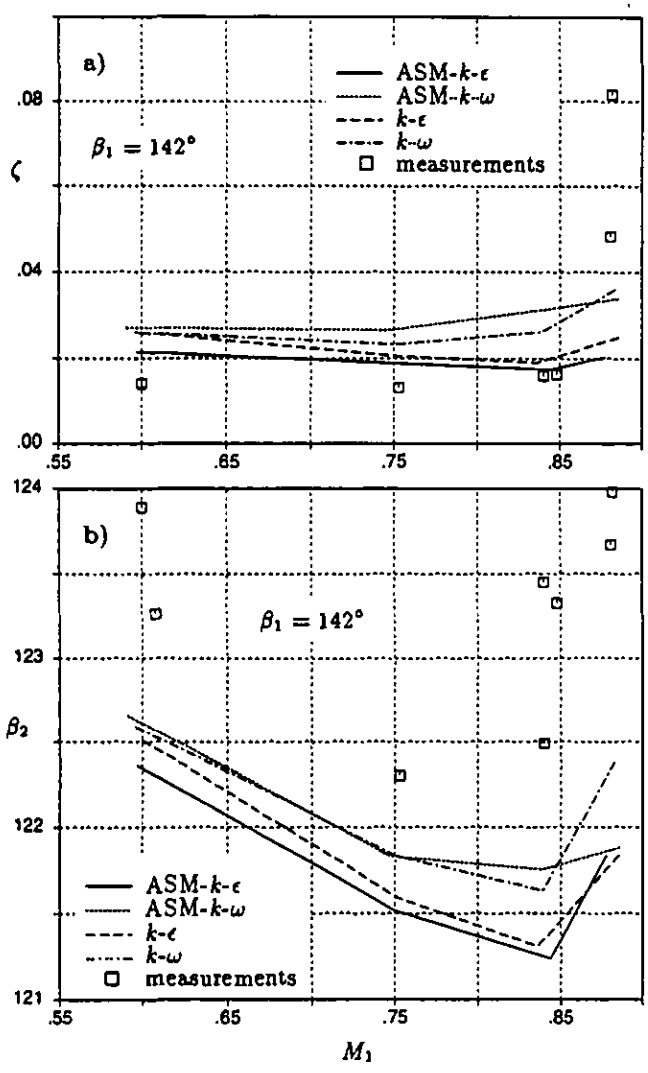

Figure 6: Dependence of the calculated and measured loss coefficient a) and exit flow angle b) on the inlet Mach number

els due to their lower boundary layer thickness in the rear half of suction side which can be seen by the Mach number distribution in Fig. (4). At design Mach number only the ASM-k-ϵ model is able to calculate the correct loss coefficient.

At $M_1 = 0.88$ the calculated losses are smaller than the measured losses corresponding to the lower isentropic Mach numbers at pressure side compared to the measurements. Especially, here at this point Ω has a considerable influence on the losses (Steinert and Starken (1996)). Both measurements differ only in their value of Ω ($\Omega = 1.14$ and $\Omega = 1.17$) and show the typical loss decrease with rising Ω.

The dependence of the exit flow angle is shown in Fig. (6h). The turbulence models differ at most by only 0.5 degree and are nearly one degree below the measurements. All models show the same characteristcs compared to the measurements with the largest deviation angle at design Mach number.

Influence of incidence angle

In Fig. (7) four isentropic Mach number distributions at increasing inlet flow angle with inlet Mach numbers near to design point are plotted. Negative incidence angles cause a compression shock in the middle of the suction side. In front of the shock all turbulence models lie close together and agree well with the measurements. But behind the shock there are great differences between the models especially with large incidence angles. Fig. (7a) shows in contrast to the measurements a constant isentropic Mach number distribution near the trailing edge for the ASM-k-ω model. This distribution is connected with a complete separation caused by the shock which is only calculated by the ASM-k-ω model. For this reason, this model calculates also the highest losses.

The k-ω and ASM-k-ϵ model calculate a small closed separation hubble behind the shock and agree better with the measurements. The k-ϵ model is the only one which calculates no separation. At pressure side the models show similar Mach number distributions with a vertical displacement due to their different losses.

At $\beta_1 = 140°$ the Mach number distributions of all turbulence models are similar and agree well with the measurements. The main differences are caused by the shock. The turbulence models calculate nearly the same high isentropic Mach number in front of the shock. But only the k-ω and ASM-k-ϵ model calculate a small closed separation bubble behind the shock.

Compared to the design point in Fig. (7c) the measured inlet Mach number in Fig. (7d) at $\beta_1 = 144°$ is lower than the design Mach number so that no compression shock exists in the middle of the suction side. Furthermore, the differences between the models and the measurements at the suction side increase. The already above mentioned small separation bubble at design point calculated by the k-ϵ models disappears with rising incidence angle. At $\beta_1 = 144°$ both k-ϵ models calculate a closed separation between approximately 15 and 45 percent of chord (Fig. (8b)) which can also be seen by the flat decreasing Mach number distribution in this region. At $\beta_1 = 145°$ this separation disappears and is replaced by a shock at 20 percent of chord (Fig. (9)). In the rear half of the suction side a second complete separation developes at approximately 70 percent of chord.

In contrast to the k-ϵ models, the k-ω models calculate this compression shock at 20 percent of chord already at $\beta_1 = 144°$ but without any separation behind (Fig. (8a)). With increasing incidence angle up to $\beta_1 = 145°$ the shock becomes stronger leading to a small closed separation bubble. Similar to the k-ϵ model a complete separation has been developed at approximately 70 percent of chord which can be identified by the constant Mach number distribution in Fig. (9) near the trailing edge.

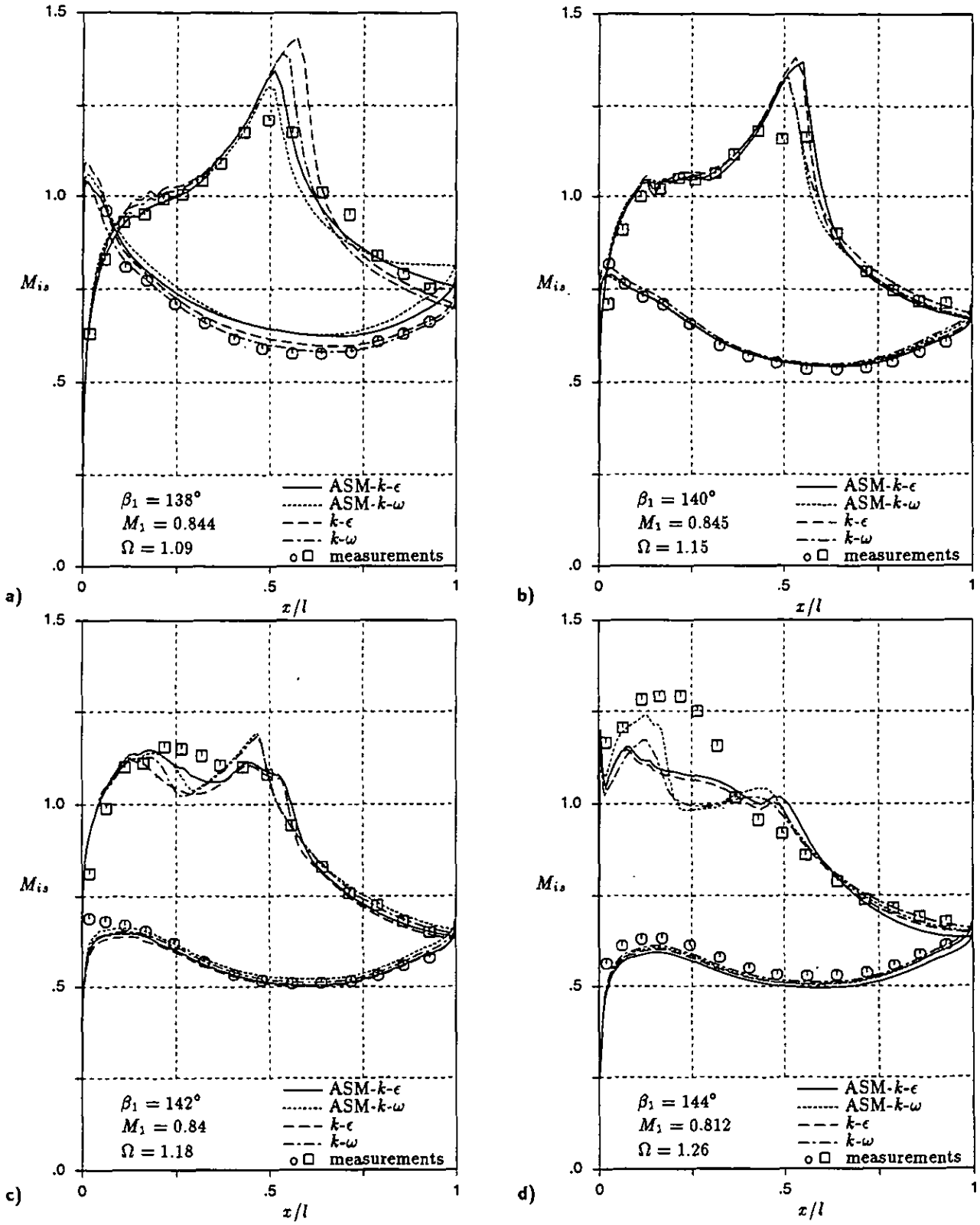

Figure 7: Isentropic surface Mach number distribution at design inlet Mach number and different incidence angels: (a) $\beta_1 = 138°$, (b) $\beta_1 = 140°$, (c) $\beta_1 = 142°$ and (d) $\beta_1 = 144°$

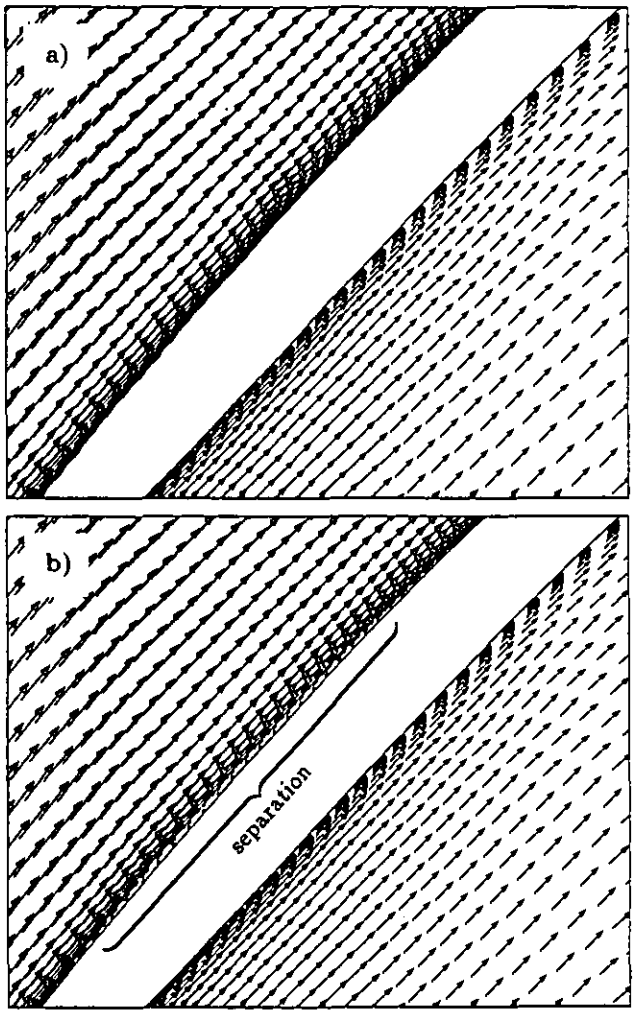

Figure 8: Velocity vectors at approximately 30 percent of chord with $\beta_1 = 144°$: a) k-ω models and b) k-ϵ models

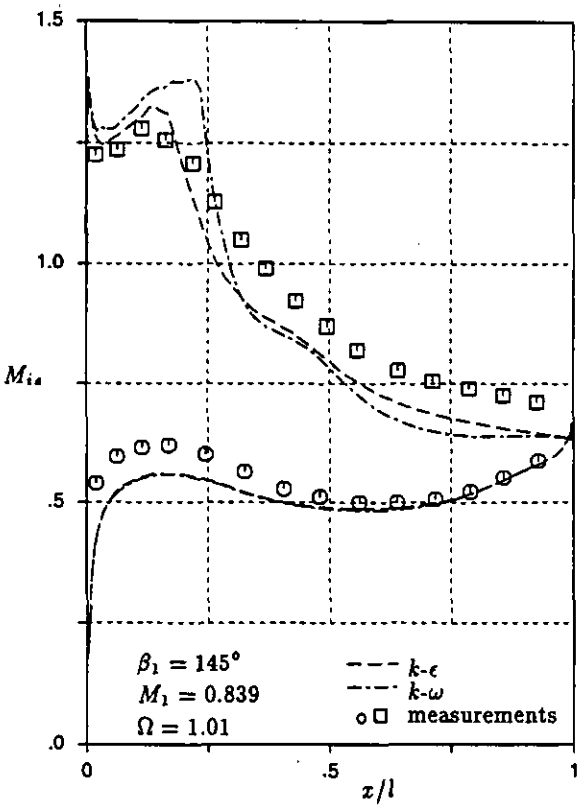

Figure 9: Isentropic surface Mach number distribution at design inlet Mach number and maximum positive incidence angle ($\beta_1 = 145°$)

At this point, the large wake region at $\beta_1 = 145°$ becomes unstable and unsteady separations are calculated, so that no comparable Mach number distributions and losses could be determined with the ASM-models. The k-ϵ and k-ω models are able to calculate a steady flow through the cascade if a local variable CFL number ($f_C = 5$ in Eq. (24)) is used. For this reason, Fig. (9) shows the Mach number distributions for these two models only.

The Mach number distributions of the ASM-models compared with their corresponding standard two-equation models are similar. For the prediction of the losses and deviation angles the structure of the flow within the boundary layer is probably responsible, so Fig. (10) shows the main differences between the models due to their different separation behaviour. At minimum negative incidence angles the ASM-models predict higher losses lying within the bandwith of the measurements and decreasing more with rising incidence angles compared to the losses of the two equation models. Especially the losses of the ASM-k-ϵ model agree very well with the measurements near the design point. With positive incidence angle the models show a contrary behavior in the prediction of the losses. Up to $\beta_1 = 144°$, the two-equation models calculate rising losses, whereas the losses of the ASM-models are nearly constant although the Mach number distributions between the corresponding k-ϵ models are quite similar. The high losses and deviation angles at $\beta_1 = 145°$ indicate the large separations at suction side and show the high dependence of the losses and deviation angles on positive incidence angles. With an incidence increase of only one degree the loss coefficient calculated by the k-ϵ model rises by a factor of 3.

CONCLUSIONS

The performance of the turbulence models to calculate the flow through a compressor cascade depends on the inlet flow conditions. The differences between the models resulting mainly from the simulation of the flow structures

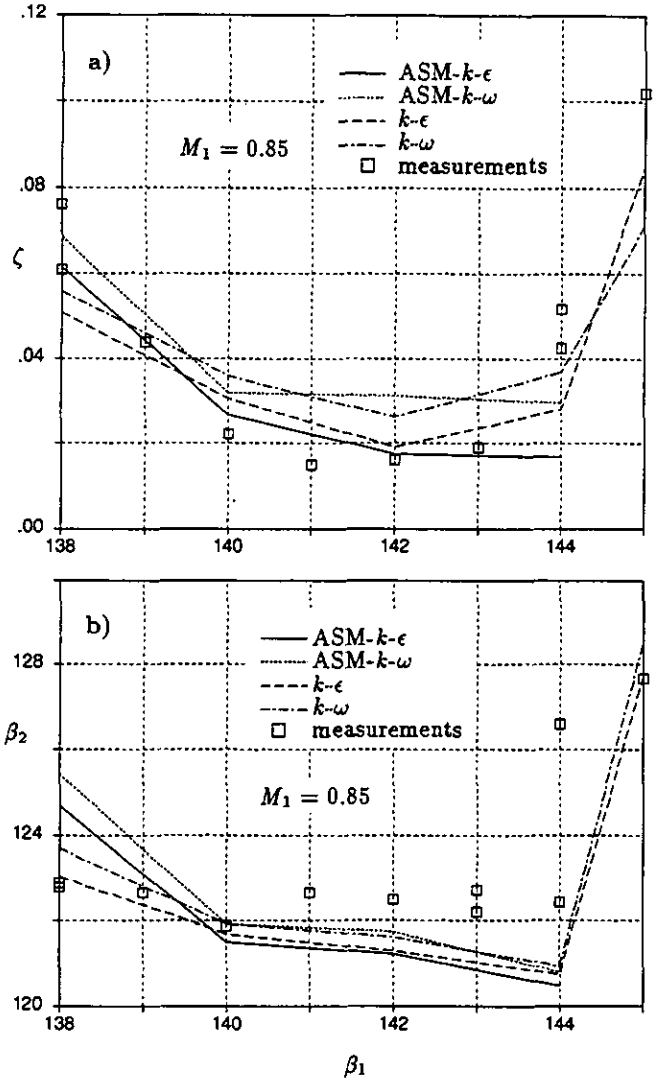

Figure 10: Dependence of the calculated and measured loss coefficient a) and exit flow angle b) on the incidence angle

within the boundary layers increase with rising Mach numbers and incidence angles. In this connection, the type of transport equations (k-ϵ or k-ω) has more influence on the losses and Mach number distributions than the type of modeled Reynolds stresses (ASM or Boussinesq concept). Due to the thinner boundary layers of the k-ϵ turbulence models these models calculate lower loss coefficients especially near the design point. Another important difference between the models is their different separation behavior within the boundary layers. The k-ϵ models are able to calculate thin separation bubbles which have no significant influence on the losses and exit flow angles but improve the predicted Mach number distributions compared to the k-ω models. In this connection the ASM-k-ϵ model shows a better agreement with the measurements compared to the low-Reynolds-Number k-ϵ model. But for a better assessment of the separation behavior of the models reliable measurements about the interaction of shocks with boundary layers are indispensable. Furthermore, for accurate simulations of compressor cascade flow more details about the distribution of the side wall boundary layers along the profile are needed.

REFERENCES

Abid, R., Rumsey, C., Gatski, T., 1995, "Prediction of Nonequilibrium Turbulent Flows with Explicit Algebraic Stress Models," *AIAA Journal*, Vol. 33, No. 11, pp. 2026–2031

Courant, R., Friedrichs, K.O., Lewy, H., 1928, "Über die partiellen Differentialgleichungen der mathematischen Physik," *Mathematische Annalen*, Vol. 100, pp. 32–74

Jawtusch, V., 1993, "Verbesserte Verlustberechnungen für die superkritischen Verdichtergitter SKG-FVV 3.3 und SKG-FVV 4.1," *FVV Forschungsberichte IB-325-07-93*

Lam, C.K.G., Bremhorst, K., 1981, "A Modified Form of the k–ϵ Model for Predicting Wall Turbulence," *Journal of Fluids Engineering* Vol. 103

Lenke, L. J., Reichert, A. W., Simon, H., 1995, "Viscous Flow Field Computations for the VKI-1 Turbine Cascade Using Different Turbulence Models," International Gas Turbine andAeroengine Congress, Houston, *ASME-Paper* 95–GT–91

Reichert, A. W., Simon, H., 1994, "Numerical Investigations to the Optimum Design of Radial Inflow Turbine Guide Vanes," International Gas Turbine and Aeroengine Congress, den Haag, *ASME-Paper* 94–GT–61

Reichert, A. W., 1995, "Strömungssimulationen zur optimierten Gestaltung von Turbomaschinenkomponenten," Hänsel-Hohenhausen, Germany

Steinert, W., Starken, H., 1996, "Off-Design Transition and Separation Behavior of a CDA Cascade," *ASME Journal of Turbomachinery*, Vol. 118, No. 4, pp. 204–210

Weber, A., et al., 1986, "Verlustarme, superkritische Schaufelgitter," *FVV-Forschungsberichte*, Nr. 325

Wilcox, D.,C., 1993, "Comparison of Two-Equation Turbulence Models for Boundary Layers with Pressure Gradient," *AIAA Journal* , Vo. 31, No. 8, pp. 1414–1421